

# Modeling of crack growth through particulate clusters in brittle matrix by symmetric-Galerkin boundary element method

R. Kitey · A.-V. Phan · H. V. Tippur · T. Kaplan

Received: 29 September 2005 / Accepted: 15 February 2006  
© Springer Science+Business Media B.V. 2006

**Abstract** The interaction of a crack with perfectly bonded rigid isolated inclusions and clusters of inclusions in a brittle matrix is investigated using numerical simulations. Of particular interest is the role inclusions play on crack paths, stress intensity factors (SIFs) and the energy release rates with potential implications to the fracture behavior of particulate composites. The effects of particle size and eccentricity relative to the initial crack orientation are examined first as a precursor to the study of particle clusters. Simulations are accomplished using a new quasi-static crack-growth prediction tool based on the symmetric-Galerkin boundary element method, a modified quarter-point crack-tip element, the displacement correlation technique for evaluating SIFs, and the maximum principal stress criterion for crack-growth direction prediction. The numerical simulations demonstrate a complex interplay of crack-tip

shielding and amplification mechanisms leading to significant toughening of the material.

**Keywords** Crack growth · Crack-inclusion interaction · Crack deflection · Particulate composites · Matrix toughening · Symmetric-Galerkin boundary element method

## 1 Introduction

Particle filled polymers are useful in a variety of engineering applications—as light-weight structural composites, as conducting polymers, as potting compounds in electronic packages, as syntactic foams for civil and marine structures, surface coats/paints for thermal insulation, to name a few. Higher stiffness and fracture toughness compared to unfilled (neat) matrix material are some of the positive mechanical attributes derived by reinforcing a matrix with stiff fillers. A favorable increase in failure properties occurs in the presence of secondary phases due to crack tip shielding, crack deflection and twisting, and crack tip blunting mechanisms. Filler particle size, shape and volume fraction, the properties of constituent phases and filler–matrix interface strength influence the toughening mechanisms and in turn the failure properties. The experimental results of particle size and filler–matrix adhesion effects on fracture behavior of heterogeneous media is a motivating factor for the current study. Spanoudakis and Young (1984a, b) observed a decrease in fracture

---

R. Kitey · H. V. Tippur  
Department of Mechanical Engineering,  
Auburn University,  
Auburn, AL 36849, USA

A.-V. Phan (✉)  
Department of Mechanical Engineering,  
University of South Alabama,  
Mobile, AL 36688, USA  
e-mail: vphan@jaguar1.usouthal.edu

T. Kaplan  
Computer Science and Mathematics Division,  
Oak Ridge National Laboratory,  
Oak Ridge, TN 37831, USA

toughness with increasing particle size for particles of sizes 4–62  $\mu\text{m}$  in diameter at low volume fractions. Unlike the monotonic trend in fracture toughness with particle size, a minimum energy release rate (ERR) was observed for 47  $\mu\text{m}$  particles. They also suggested that poor inclusion–matrix bonding causes an increase in ERR. Crack pinning followed by crack tip blunting was anticipated to be the potential toughening mechanism. Moloney et al. (1987) reported that for the particle sizes ranging from 60 to 300  $\mu\text{m}$ , fracture toughness has negligible variation but weaker filler–matrix interface does increase the fracture toughness due to possible crack tip blunting. On the contrary, Nakamura et al. (1999), Nakamura and Yamaguchi (1992) noticed prominent increase in fracture toughness with increasing particle size for the sizes ranging from 2 to 42  $\mu\text{m}$ . The increased crack deflection, interfacial debonding and particle fracture were suggested as reasons for the increased fracture toughness. They also concluded that fracture toughness is unaffected by filler–matrix adhesion strength. The contrasting results among previous studies, possibly due to the narrow range of particle sizes were addressed by Kitey and Tippur (2005a, b) recently. They observed a non-monotonic bell shaped variation in fracture toughness for 7–200  $\mu\text{m}$  particle sizes. They observed localized crack tip blunting and crack front trapping as potential toughening mechanisms when filler particles were weakly bonded to the matrix. For strongly bonded particles, on the other hand, fracture toughness values were consistently lower compared to the weakly bonded components. They have attributed this difference to the crack front getting trapped at weak filler–matrix interfaces causing localized blunting and crack growth retardation. The weaker interfaces also act as distributed attractors driving the crack into modes II and III conditions in addition to the dominant mode I, thereby increasing the crack path tortuosity.

A few previous works have tried to explain toughening mechanisms using analytical and numerical studies. Atkinson (1972) calculated the stress field around a crack tip for a symmetrically located crack in the presence of an inclusion. He concluded that inverse  $\sqrt{r}$  singularity exists for crack positions up to a distance very close to the inclusion until the crack is not touching the inclusion. In a similar investigation Erdogan et al. (1974) calculated the generalized stress field around the crack tip and stress intensity factors (SIFs) using Green's function for an arbitrarily oriented crack with

respect to a circular inclusion. A model predicting an increase in fracture toughness due to crack deflection and twisting around a secondary phase filler is proposed by Faber and Evans (1983). They have shown the dependence of fracture toughness on morphology and volume fraction of the secondary phase, while the fracture toughness is shown to be invariant relative to particle size.

There have been several analytical and numerical studies on the topic. Analytical approaches have been developed for problems concerning cracks along the interface of various types of inclusions (e.g., Tamate 1968; Sendekyj 1974; Hwu et al. 1995). Numerical techniques, including finite element method (e.g., [Li and Chudnovsky 1993a,b Ferber et al. 1993; Lipetzky and Schmauder 1994; Lipetzky and Knesl 1995; Haddi and Weichert 1998]) and boundary element method (BEM) (e.g., [Bush 1997; Knight et al. 2002; Wang et al. 1998]), have been employed to investigate this type of fracture behavior under static loading conditions. Recently, the dynamic response of the interaction between a crack and an inclusion using the time-domain BEM has been studied by Lei et al. (2005). Note that the dual BEM (DBEM) is used in Bush (1997) and Knight et al. (2002) while the sub-domain BEM technique is adopted in Wang et al. (1998) and Lei et al. (2005). Li and Chudnovsky (1993) have numerically shown that when a crack approaches a rigid inclusion in a relatively compliant matrix, the crack tip is shielded from the far-field stresses. This decreases stress intensification at the crack tip and hence lowers the ERR. They also show that typically, a crack tip gets shielded when the crack approaches an inclusion while stresses are amplified when the crack propagates away (departs) from the particle. Bush (1997) has investigated the effect of single inclusion and an inclusion cluster on crack trajectory and energy release rate. He considered two different types of inclusions in his simulations; ones which were perfectly bonded to the matrix and the others with interface flaws or partially bonded to the matrix. He showed that pre-existing flaws on inclusion–matrix interface attract the propagating crack. The crack deflection around an inclusion is noticed when the crack tip is one radius away from the inclusion. Knight et al. (2002) examined crack deflection/attraction mechanisms in a crack–particle interaction investigation by performing a series of parametric studies for different Young's modulus and Poisson's ratio mismatches. For the inclusions with and without interphase regions between filler and matrix,

Poisson’s ratio was shown to significantly affect crack trajectories.

The key feature of the BEM approach is that only the boundary of the domain is discretized and only boundary quantities are determined. It is generally recognized that the BEM is particularly well suited for linear elastic fracture mechanics, as the method is known to provide more accurate results for stress and there is no need for re-meshing the boundary during the modeling of crack propagation. Recently, the symmetric-Galerkin boundary element method (SGBEM) has been developed (e.g., Bonnet 1995; Bonnet et al. 1998) and has shown several key advantages in fracture applications: (a) as the name implies, SGBEM formulation results in a symmetric coefficient matrix; (b) the presence of both displacement and traction BIE enables fracture problems to be solved without using artificial sub-domains; (c) unlike BEM or DBEM, there is no smoothness requirement on the displacement (e.g., Gray 1991; Martin and Rizzo 1996) in order to evaluate the hypersingular integral; thus, standard *continuous* and quarter-point (QP) elements can be employed.

In both finite and boundary element fracture modeling, the standard approach consists of incorporating the  $\sqrt{r}$  displacement behavior at the crack tip by means of the QP element (Henshell and Shaw 1975; Barsoum 1976), where  $r$  is the radial distance from the crack tip. Recently, Gray and Paulino (1998) have proved that, for an arbitrary crack geometry, a constraint exists in the series expansion of the crack opening displacement (COD) at the tip. As discussed in Gray and Paulino (1998), the QP element in general fails to satisfy this constraint, and this has led to the development of an improved modified quarter-point (MQP) element (Gray et al. 2003). It was demonstrated in Gray et al. (2003) that the accuracy of the computed SIFs using the Displacement Correlation Technique (DCT) can be significantly improved by incorporating this MQP element into the SGBEM. This suggests that stress methods such as the maximum principal stress criterion (MPSC) (Erdogan and Sih, 1963) can effectively be used as the criteria for crack-growth direction in a quasi-static crack-growth prediction tool made up from the SGBEM, the MQP, and the DCT.

The focus of this paper is on simulations of crack-growth through particulate polymer matrix composites. Of interest is the study of the effects of inclusion size, eccentricity and crack tip shielding on crack path and SIF, and the effects of particle arrangement and volume

fraction on the ERR of a brittle particulate composite such as glass-filled epoxy. The simulations are carried out using the crack-growth prediction tool mentioned above. The performance of the tool is bench marked by running crack growth simulations in an unfilled or neat matrix and comparing the obtained SIF variation with an available analytical solution. It is shown from this work that, even with a simple local SIF method such as the DCT, and a simple stress method for crack growth direction, the proposed numerical tool is able to capture complex interplay of crack–tip shielding and amplification mechanisms for various crack–inclusion interaction situations.

## 2 A Crack-growth prediction tool

### 2.1 SGBEM fracture analysis

This section provides a very brief review of the SGBEM and its application to fracture. The reader is asked to consult the cited references for further details.

Consider a domain  $B$  containing a crack  $\Gamma_c = \Gamma_c^+ + \Gamma_c^-$  on which only tractions are prescribed and  $\tau_c^+ = -\tau_c^-$  (Fig. 1). The boundary integral equation (BIE) without body forces for linear elasticity is given by Rizzo (1967). For a source point  $P$  interior to the domain, if the displacements  $u_c^+$  and  $u_c^-$  are replaced by the COD  $\Delta u_c = u_c^+ - u_c^-$  on  $\Gamma_c^+$ , and note that  $\tau_c^+ + \tau_c^- = 0$ , the BIE is written as

$$\begin{aligned} \mathcal{U}(P) &= u_k(P) \\ &- \int_{\Gamma_b} [U_{kj}(P, Q) \tau_j(Q) - T_{kj}(P, Q) u_j(Q)] dQ \\ &+ \int_{\Gamma_c^+} T_{kj}(P, Q) \Delta u_j(Q) dQ = 0, \end{aligned} \tag{1}$$

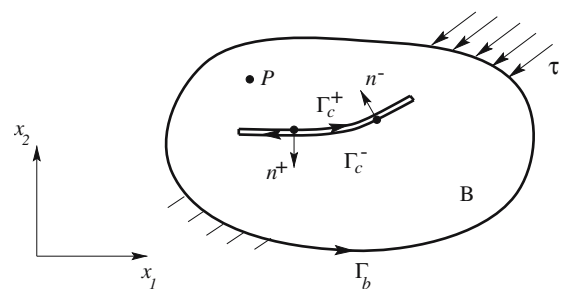


Fig. 1 A body  $B$  containing a crack

where  $Q$  is a field point,  $\tau_j$  and  $u_j$  are traction and displacement vectors,  $U_{kj}$  and  $T_{kj}$  are the Kelvin kernel tensors or fundamental solutions,  $\Gamma_b$  denotes the outer boundary of the domain, and  $dQ$  is an infinitesimal boundary length (for 2-D) or boundary surface (for 3-D cases).

It can be shown that the limit of the integral in Eq. (1) as  $P$  approaches the boundary exists. From now on, for  $P \in \Gamma = \Gamma_b + \Gamma_c$ , the BIE is understood in this limiting sense.

As  $P$  is off the boundary, the kernel functions are not singular and it is permissible to differentiate Eq. (1) with respect to  $P$ , yielding the hypersingular BIE (HBIE) for displacement gradient. Substitution of this gradient into Hooke’s law gives the following HBIE for boundary stresses:

$$\begin{aligned} \mathcal{S}(P) &= \sigma_{k\ell}(P) \\ &- \int_{\Gamma_b} [D_{kj\ell}(P, Q)\tau_j(Q) - S_{kj\ell}(P, Q)u_j(Q)] dQ \\ &+ \int_{\Gamma_c^+} S_{kj\ell}(P, Q) \Delta u_j(Q) dQ = 0. \end{aligned} \tag{2}$$

Expressions for the kernel tensors  $U_{kj}$ ,  $T_{kj}$ ,  $D_{kj\ell}$  and  $S_{kj\ell}$  can be found in Bonnet (1995).

The Galerkin boundary integral formulation is obtained by taking the shape functions  $\psi_m$  employed in approximating the boundary tractions and displacements as weighting functions for the Eqs. (1) and (2). Thus,

$$\int_{\Gamma} \psi_m(P) \mathcal{U}(P) dP = 0, \tag{3}$$

$$\int_{\Gamma} \psi_m(P) \mathcal{S}(P) dP = 0. \tag{4}$$

A symmetric coefficient matrix, and hence a symmetric-Galerkin approximation, is obtained by employing Eq. (3) on the boundary  $\Gamma(\mathbf{u})$  where displacements  $u_{bv}$  are prescribed, and similarly Eq. (4) is employed on the boundary  $\Gamma(\boldsymbol{\tau})$  with prescribed tractions  $\tau_{bv}$ . Note that  $\Gamma = \Gamma(\mathbf{u}) + \Gamma(\boldsymbol{\tau})$ . The additional boundary integration is the key to obtain a symmetric coefficient matrix, as this ensures that the source point  $P$  and field point  $Q$  are treated in the same manner.

### 2.2 Modified quarter-point element

The 2-D QP element is based upon the three-equidistant-noded quadratic element. For  $t \in [0, 1]$ , the shape functions for this element are given by

$$\begin{aligned} \psi_1(t) &= (1 - t)(1 - 2t), \\ \psi_2(t) &= 4t(1 - t), \\ \psi_3(t) &= t(2t - 1). \end{aligned} \tag{5}$$

As mentioned in the Introduction, this QP element fails to satisfy a constraint in the series expansion of the COD at the crack tip (Gray and Paulino, 1998). A remedy was presented in Gray et al. (2003) and this results in the following MQP shape functions ( $\hat{\psi}_1(t)$  is not required as  $\Delta \mathbf{u} = 0$  at the crack tip):

$$\begin{aligned} \hat{\psi}_2(t) &= -\frac{8}{3}(t^3 - t), \\ \hat{\psi}_3(t) &= \frac{1}{3}(4t^3 - t). \end{aligned} \tag{6}$$

It can be observed that the modified shape functions (6) still satisfy the Kronecker delta property  $\hat{\psi}_i(t_j) = \delta_{ij}$ . This new approximation is only applied to the COD, as we must use the standard shape functions (5) for the representation of the crack tip geometry. This ensures that the property  $t \sim \sqrt{r}$  remains.

### 2.3 Stress intensity factors by the DCT

There are several approaches for numerically evaluating SIFs. Among these approaches, the DCT based upon the COD in the vicinity of the crack tip is a very simple method. In case of using the MQP element, the expressions for SIFs by means of the DCT are given by (Gray et al., 2003)

$$\begin{aligned} K_I &= \frac{\mu}{3(\kappa + 1)} \sqrt{\frac{2\pi}{L}} \left( 8\Delta u_2^{(2)} - \Delta u_2^{(3)} \right), \\ K_{II} &= \frac{\mu}{3(\kappa + 1)} \sqrt{\frac{2\pi}{L}} \left( 8\Delta u_1^{(2)} - \Delta u_1^{(3)} \right). \end{aligned} \tag{7}$$

where  $\mu$  is the shear modulus,  $\nu$  is Poisson’s ratio, and

$$\begin{aligned} \kappa &= 3 - 4\nu \text{ (plane strain)}, \\ \kappa &= \frac{3 - \nu}{1 + \nu} \text{ (plane stress)}. \end{aligned} \tag{8}$$

Since SIFs are directly given in terms of the nodal values of the COD at the crack tip element, the use of MQP element herein is highly beneficial as it would enhance the accuracy of the nodal CODs, thus the accuracy of the obtained SIFs. Further, energy release rate  $G$  is calculated using SIFs by,

$$G = \frac{\kappa + 1}{8\mu} (K_I^2 + K_{II}^2). \tag{9}$$

## 2.4 Maximum principal stress criterion

There are several criteria for predicting crack growth direction (e.g., Erdogan and Sih, 1963; Sih, 1974). The MPSC proposed by Erdogan and Sih (1963) is adopted herein. According to this criterion, the crack growth direction  $\theta_c$  is perpendicular to that of the maximum principal stress, and the crack will propagate when  $K_I$  exceeds the fracture toughness  $K_{Ic}$  of the material.

Since in the direction  $\theta_c$ ,  $\sigma_{r\theta} = 0$ , i.e.

$$\sigma_{r\theta} = K_I \sin \theta_c + K_{II} (3 \cos \theta_c - 1) = 0 \quad (10)$$

thus,

$$\theta_c = 2 \tan^{-1} \left( \frac{K_I}{4K_{II}} \pm \frac{1}{4} \sqrt{\left( \frac{K_I}{K_{II}} \right)^2 + 8} \right). \quad (11)$$

A quasi-static crack-growth prediction tool based upon the SGBEM, the MQP crack-tip element, the DCT and the MPSC is employed for the simulations conducted in this work. By incorporating the MQP shape functions (6) into a SGBEM code, accurate CODs  $\Delta \mathbf{u}$  at the mid and end nodes of any crack-tip element may be obtained (see Eqs. (1) and (2)). The SIFs at the crack tip of interest will then be evaluated by substituting the related CODs in the DCT formulas (7). If  $K_I \geq K_{Ic}$  the crack-growth direction  $\theta_c$  of the crack tip in question is determined by Eq. (11), and an infinitesimal crack increment is added in that direction during the simulation. As a result, remeshing a propagating crack is straightforward. Only a new crack-tip element needs to be added in the crack-growth direction  $\theta_c$  while the previous element discretization remains unchanged. At issue is obviously the size of the new crack-tip element. Smaller sizes, although leading to more time-consuming simulations, are expected to result in more accurate results.

## 3 Simulation results and discussion

To investigate the effects of particle arrangement and volume fraction on crack and particle-cluster interaction, a plane stress situation involving a cracked sheet of dimensions 140 mm  $\times$  40 mm  $\times$  8 mm is considered<sup>1</sup>. The material properties of the matrix and inclusions

<sup>1</sup> The dimensions are chosen with future experimental simulations involving optical interferometry in mind (Kitey and Tippur, 2005a)

are matched with those for epoxy and glass, respectively, with an elastic modulus ( $E$ ) 3.2 GPa and Poisson's ratio ( $\nu$ ) 0.3 for epoxy and  $E = 70$  GPa,  $\nu = 0.3$  for glass. The loading configuration considered in all simulations is one of 3-point bending of an edge cracked sheet/beam. A crack is located at the edge of the sheet opposite to the loading point and along the loading axis. The line joining the initial crack tip and loading point is referred to as line-of-symmetry throughout the article.

### 3.1 Benchmarking and mesh convergence

To ensure a high degree of accuracy of SIFs calculated by BE simulations, first a single edge notched geometry (see inset in Fig. 2(a)) of neat matrix material without any inclusions is carried out. The geometry is a symmetrically loaded 3-point bend configuration. The initial crack length is chosen such that  $a/W = 0.25$  where  $W$  is the total width of the chosen geometry. In the simulations, equal length boundary elements are used to represent specimen edges including the initial crack. This length is determined first by performing a convergence study. The SIF results for different element lengths varying from  $W/10$  to  $W/40$  as a function of crack length are determined for a symmetrically loaded 3-point bend configuration using [Anderson 1995],

$$K_I = \frac{3 \frac{PL}{BW^2} \sqrt{a}}{2 \left(1 + 2 \frac{a}{W}\right) \left(1 - 2 \frac{a}{W}\right)^{3/2}} \left[ 1.99 - \frac{a}{W} \left(1 - \frac{a}{W}\right) \times \left\{ 2.15 - 3.93 \frac{a}{W} + 2.7 \left(\frac{a}{W}\right)^2 \right\} \right]. \quad (12)$$

Non-dimensional SIF ( $= K_I \frac{B\sqrt{W}}{P}$ ) values from SGBEM are compared with analytical results in Fig. 2(a) for different  $a/W$  ratios. With a decrease in element length accuracy of SIF calculations increase. Good agreement between calculated  $K_I$  values using SGBEM and analytical results are evident when an element length of  $W/40$  is used. For this choice, a high degree of accuracy can be expected up to  $a/W = 0.75$  with an error less than 2.5%. Beyond  $a/W = 0.75$ , however, the accuracy reduces due to the dominance of loading point stresses on the crack tip stress field.

Next, the crack tip increment length in the direction of propagation is determined separately to match experimentally determined crack paths in a mixed-mode

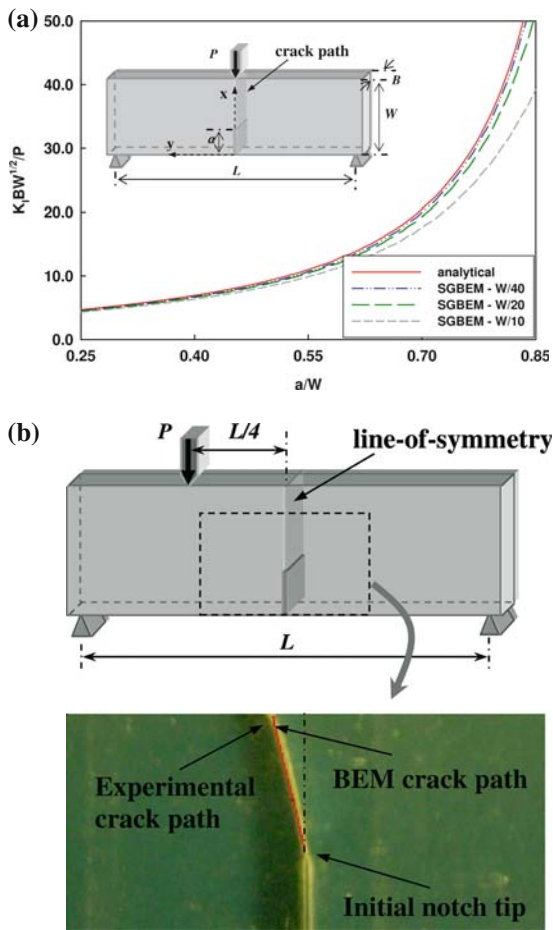


**Fig. 2** (a) Comparison between the analytical results and SGBEM results for various boundary element lengths, (b) Crack propagation for mixed-mode loading; crack trajectory from BEM is superimposed on experimentally obtained crack path for an eccentrically applied load at the distance  $L/4$  from the line-of-symmetry

loading situation. The crack geometry used in the simulations is the same as shown earlier for the mode-I case (Fig. 2(a)), except for the location of the applied load. The loading point is at a distance of  $L/4$  from the line-of-symmetry, where  $L$  is the span. Various crack tip increments were used before choosing  $\Delta a/W = 6.25 \times 10^{-3}$  in the simulations. The loading configuration, specimen geometry and the fractured epoxy specimen from an experiment are shown in Fig. 2(b). The crack trajectory from BE analysis is superimposed on experimentally obtained crack path. Excellent agreement between crack paths shows the accuracy of SGBEM in capturing mode-mixity using the chosen crack tip increment.

### 3.2 Crack tip shielding

Next, crack growth is simulated in the presence of a rigid inclusion in the crack path. When inclusions are perfectly bonded to the matrix material, crack deflection is a prominent toughening mechanism. The crack deflection depends on inclusion size, inclusion eccentricity with respect to the crack orientation, the number of inclusions surrounding the crack tip, etc. As mentioned earlier, a rigid inclusion in a relatively compliant matrix shields the crack tip as it is approached. However, the shielding depends on the location of the inclusion with respect to the initial crack orientation. Also, the particle size, particle eccentricity, the number of particles and arrangement of particles around the crack tip are some of the other parameters which affect the degree of shielding.

First a case when a cylindrical inclusion of diameter  $d = W/10$  is symmetrically located in front of a crack tip is considered. In this, the inclusion is located in front of the initial crack tip at  $p/W = 0.65$ , where  $p$  is the distance of the center of the inclusion in the  $x$ -direction (see Fig. 3(a)). The plot in Fig. 3(b) shows the variation of nondimensional  $K_I$  with crack length  $a/W$ . For comparison the  $K_I$  variation for the case of the neat matrix is also shown. A sharp decrease in SIF can be noticed from the plot as the crack approaches the inclusion. The inclusion in front of the crack shows a negligible effect on  $K_I$  until the crack reaches a length of approximately  $a/W = 0.45$ . This suggests that the presence of rigid inclusion in front of the crack is felt only when the tip is at the distance of  $\approx 1d$  from the inclusion. When the crack is  $d/4$  away from the inclusion,  $K_I$  decreases substantially. The  $K_I$  approaches zero as the crack propagates further and reaches the inclusion.

The accuracy of ERR calculations were validated against the results reported in Ref. [Bush 1997]. The geometry and loading configuration (see Figs. 3 and 7 in [Bush 1997]) is shown in Fig. 4(a). The inclusion radius  $r$  is considered as  $L/20$ , where  $L$  is the length of the planar body with an edge crack. The ratio of the elastic moduli  $E_p/E_m$  is varied from 2 to 8, where the subscripts  $p$  and  $m$  correspond to the inclusion and the matrix, respectively. The Poisson's ratio for the inclusion and matrix are considered as 0.33 and 0.17, respectively. In Fig. 4(b) nondimensional ERR,  $G/G_0$ , is plotted with varying nondimensional crack lengths, where  $G_0$  is the ERR for the matrix. The crack tip shielding

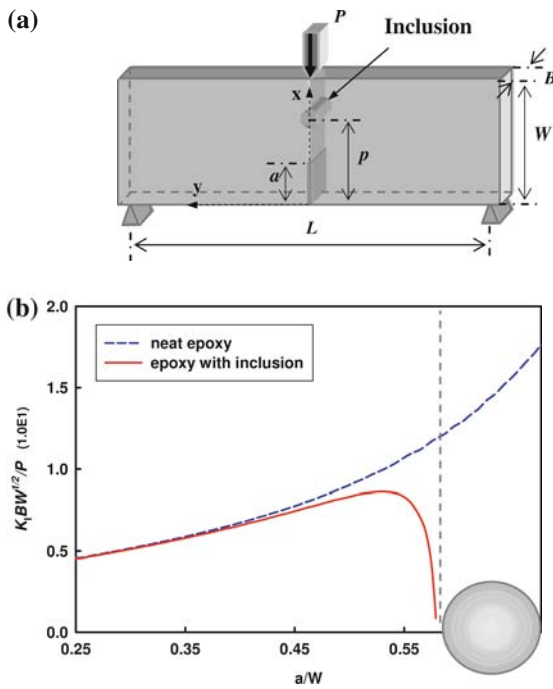


**Fig. 3** Crack tip shielding by a rigid inclusion in front of a mode-I crack: (a) Loading configuration; (b) Comparison between SIF variations in the presence and absence of inclusion

increases (i.e.,  $G/G_0$  decreases) with increasing  $E_p/E_m$ . The crack senses the rigid particle in front of it at least from a distance of  $\approx 5$  radii. The observed  $G/G_0$  variations for various  $E_p/E_m$  are same as the ones reported by Bush 1997) and hence suggests the accuracy of ERR calculations from SGBEM in the presence of secondary phases. Minor differences in ERR value, when the crack reaches the particle can be attributed to the different methods of ERR calculation (DCT method in current study).

The crack tip shielding and amplification effects are further explored by simulating a mode-I problem with a pair of inclusions ahead of a propagating crack. A *symmetrically* located pair of inclusions with respect to the crack orientation, as shown in Fig. 5, leads to crack growth under mode-I conditions. Here the inclusions are located at  $p/W = 0.5$  or,  $W/4$  away in the  $x$ -direction from the initial crack tip. The separation distance 's' between inclusions is varied from  $d/8$  to  $2d$ , where  $d = W/10$ . Figure 5 shows the variation of  $G/G_0$  with  $a/W$ .

Denoting the inclusion location (the orientation of the center of the inclusion(s)) in the  $x$ -direction as  $p/W$ ,

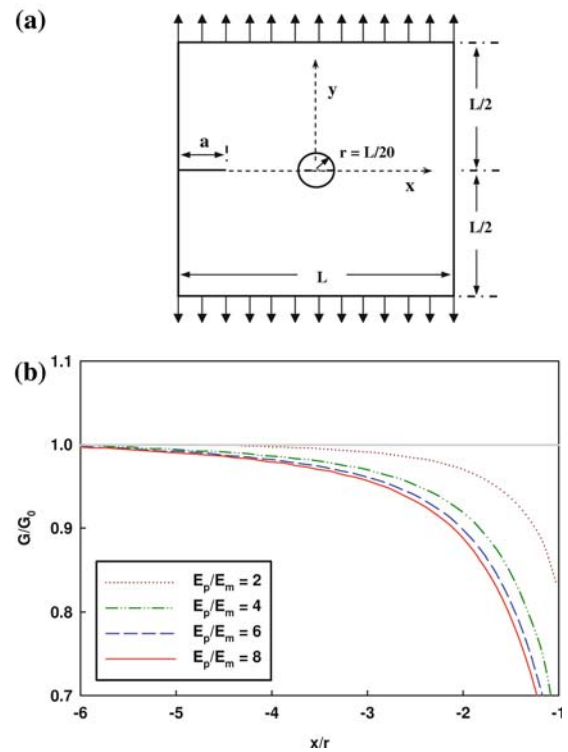


**Fig. 4** Validation of ERR calculation from SGBEM in the presence of secondary phase filler, (a) Problem geometry and loading configuration, (b) Variation of non-dimensional ERR for various  $E_p/E_m$ ,  $\nu_p = 0.17$ ,  $\nu_m = 0.33$

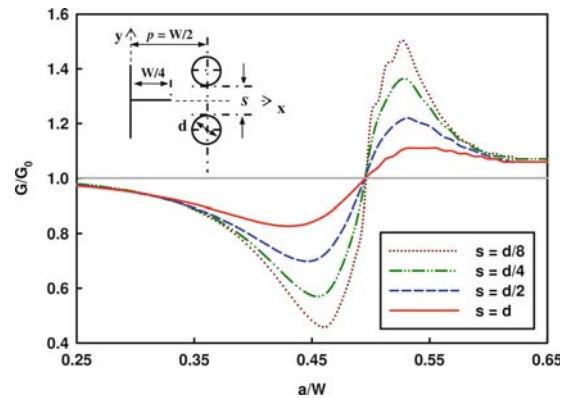


**Fig. 5** Crack tip shielding and amplification effects due to a pair of symmetrically situated inclusions in the crack path

it is evident that as the crack length approaches  $p/W$ , crack tip shielding effects begin to manifest as decreasing ERR ( $G/G_0 < 1$ ) values with  $a/W$ . It can be noticed that maximum shielding occurs when the crack tip is approximately  $d/2$  in front of the center of the inclusion.

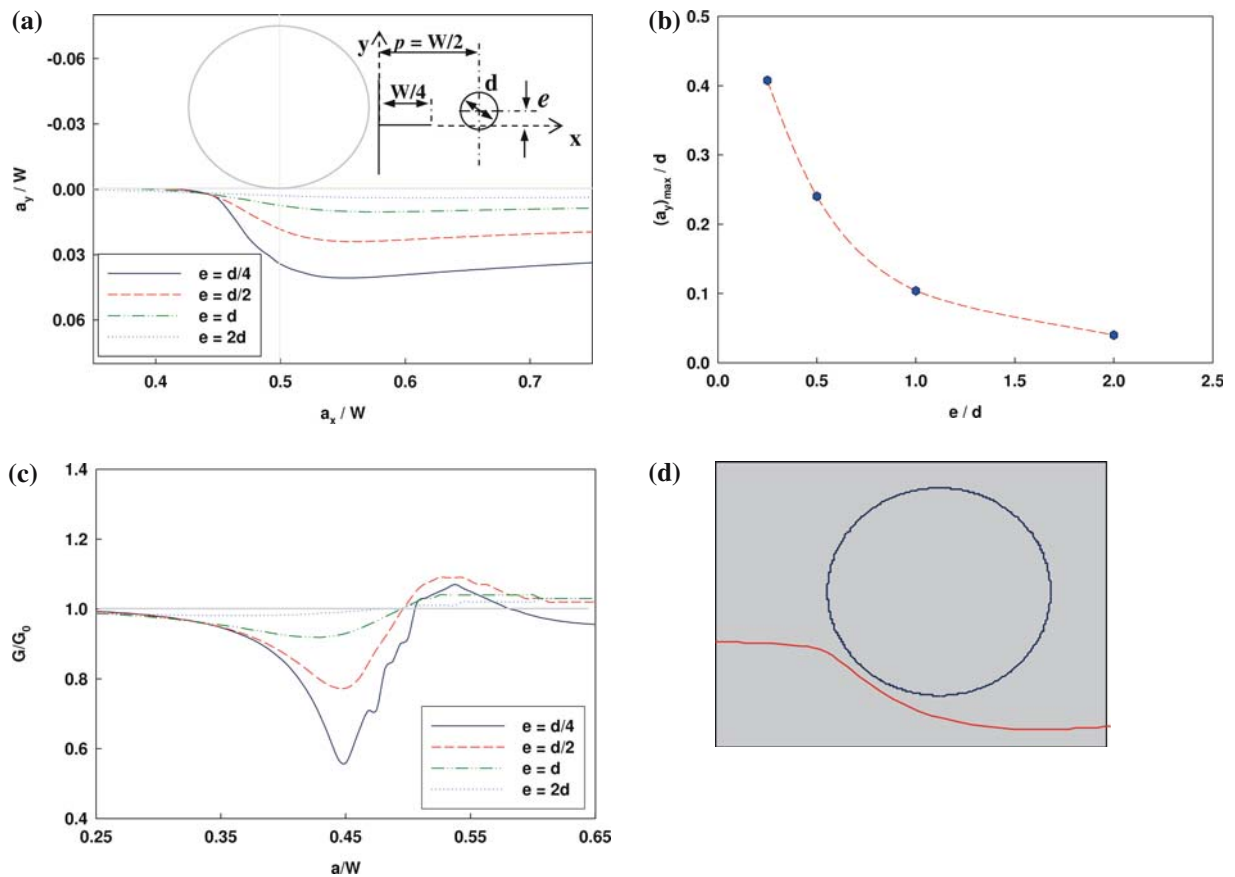


**Fig. 6** The effect of eccentrically situated rigid inclusions relative to the initial crack on crack deflection and energy release rate; (a) Crack deflection with varying inclusion eccentricity; the inclusion location is shown with respect to initial crack orientation; (b) Variation of maximum crack deflection from the line-

of-symmetry with inclusion eccentricity for inclusion diameter  $d = W/10$ ; (c) Variation in nondimensional ERR with  $a/W$ ; (d) Crack propagation around a rigid inclusion from SGBEM simulation

Further crack propagation decreases shielding. That is, the nondimensional ERR reaches a value of unity when the propagating crack length  $a/W$  reaches  $p/W$ . As the crack propagates beyond  $p/W$ , an amplification of ERR ( $G/G_0 > 1$ ) values can be seen. The maximum amplification is seen when the crack tip is at a distance of  $d/2$  away from the center of the inclusion. The amplification begins to vanish as the crack propagates away from this location. The above crack shielding/amplification effects are similar to the ones reported in Refs. [Li and Chudnovsky 1993; Bush 1997].

From the plots in Fig. 5 it can also be seen that the shielding/amplification effect increases as the inclusion separation distance decreases. The effects are quite evident even when the inclusions are  $2d$  apart. Interestingly, the magnitude of maximum shielding is always

greater than the magnitude of maximum amplification for a given value of  $s$ . If one were to associate the decrease in inclusion separation as a measure of increase in filler volume fraction, these results suggest that even at low volume fractions shielding effects are significant and the effect increases as the filler volume fraction increases.

### 3.3 Particle eccentricity effect

Next, interaction between a crack and an isolated inclusion located eccentrically to the initial crack is investigated. Of particular interest is the role inclusion eccentricity plays on crack deflection and the resulting ERR variation during crack growth. As shown in

Fig. 6(a), the center of the inclusion is located  $W/4$  away from the initial crack tip in the  $x$ -direction. The inclusion eccentricity ' $e$ ' (the distance between the center of the inclusion and the line-of-symmetry) is varied from  $d/4$  to  $2d$  while the load is applied symmetrically in a 3-point bend configuration as before. The crack paths around inclusions for different values of eccentricity are shown in Fig. 6(a). In these simulations, the crack propagates nearly in a mode-I fashion until the tip reaches  $a/W \approx 0.45$  or  $\approx 1d$  in front of the center of the inclusion. As the crack propagates further, the angle of deflection<sup>2</sup> increases. A sharp increase in the angle of deflection can be noticed from  $a/W \approx 0.45$  onwards, when the crack is  $d/2$  behind the the center of the inclusion. The angle of deflection attains a maximum value at  $a/W \approx 0.475$ . This is followed by a decrease in the angle of deflection with the crack still propagating away from the line-of-symmetry. When the crack travels  $\approx d/2$  away from the particle location  $p/W$ , the crack begins to propagate towards the line-of-symmetry with a relatively small angle of deflection. Plots suggest that the crack deflection increases as the eccentricity decreases. A symmetrically oriented inclusion ( $e = 0$ ) can be viewed as a limiting case when the crack gets stalled at the inclusion–matrix interface (see Fig. 3(b)). The variation of maximum crack deflection with inclusion eccentricity is shown in Fig. 6(b). From the plot it appears that the maximum crack deflection increases exponentially with decreasing eccentricity.

The effect of inclusion eccentricity on ERR is presented in Fig. 6(c). The figure shows the variation of nondimensional ERR,  $G/G_0$ , with  $a/W$ . It can be seen from the plots that ERR decreases as the crack approaches the inclusion. The minimum value of ERR occurs when  $a/W \approx 0.45$  or when the crack tip is located  $\approx d/2$  behind the the center of the inclusion. With further crack propagation, ERR values increase and approach unity as  $a/W$  reaches  $p/W$ . An amplification in SIF and hence ERR can be noticed as the crack starts propagating away (recede) from the inclusion. This relatively small increase in ERR continues until crack propagates a distance of approximately  $d/2$  away from the inclusion. With further crack propagation,  $G/G_0$  decreases and asymptotically approaches unity. Similar to the effects of eccentricity on crack

deflection,  $G/G_0$  increases as the inclusion eccentricity  $e$  decreases. The maximum effect can be seen for zero eccentricity (also shown in Fig. 3(b)).

It should be emphasized here that the crack growth and ERR calculations are based on propagation occurring in the matrix material at all times. If the crack were to enter the matrix–inclusion interfacial region, crack tip fields corresponding to dissimilar material interfaces will have to be used [He and Hutchinson 1989]. Simulations reported here correspond to the crack growth occurring close to an interface yet in the matrix only as a sub-interfacial crack. An example of the same for the case of  $e = d/4$  is shown in Fig. 6(d).

For the sake of completeness, the combined effects of shielding and eccentricity are studied next using a pair of inclusions located eccentrically with respect to the line-of-symmetry (see Fig. 7). The separation distance ' $s$ ' between the inclusions is kept constant ( $s = d/2$ ) while the eccentricity of the inclusion nearest to the line-of-symmetry is varied from  $d/2$  to  $3d/4$ . The variation of crack path for various eccentricities are not shown here for brevity which showed similar eccentricity effect as for the case of single inclusion (Fig. 6(a)) with an exception of relatively small crack deflections. The variation of  $G/G_0$  with  $a/W$  is plotted in Fig. 7. Plots overlap on each other in most part except when the crack propagates between  $a/W \approx 0.4$  and  $0.5$  (i.e., from a distance  $\approx 1d$  in front of the particle center) for various eccentricities. Small but monotonic variation in minimum value of  $G/G_0$  can be noticed with increasing

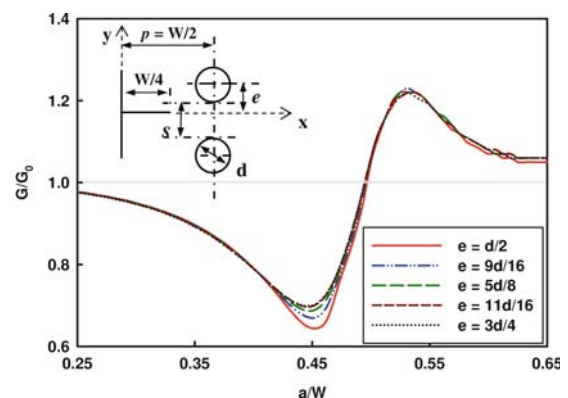


**Fig. 7** Variation of  $G/G_0$  with  $a/W$  in the presence of eccentrically located pair of inclusions showing the combined effect of shielding and inclusion eccentricity (Note: Eccentricity of the inclusion-pair is defined for the nearest inclusion center relative to the crack)

<sup>2</sup> Angle of deflection is the absolute angle between the *line-of-symmetry* (initial crack orientation) and the tangent to the crack path at any instant.

inclusion eccentricity. The lowest magnitude of  $G/G_0$  (at  $a/W \approx 0.45$ ) decreases with decrease in eccentricity, the minimum being for the case of symmetrically located pair of particles. Interestingly the eccentricity of a pair of particles is noticed to be playing negligible role on amplification.

### 3.4 Particle size effect

In this part the effect of inclusion size on crack deflection and ERR is investigated. An inclusion is located at a distance  $W/4$  away from the initial crack tip with an eccentricity of  $d/2$  (see Fig. 8(a)). The inclusion diameter is varied from  $W/40$  to  $W/5$ . The crack paths for various sizes of inclusions at  $p/W = 0.5$  is shown in Fig. 8(a). Again, the load is applied symmetrically in a 3-point bend configuration. Evidently, the crack propagates in a mode-I fashion until the inclusion is  $\approx 1d$  in front of the crack tip. As the distance between the inclusion and the crack tip decreases, crack deflection increases. The angle of deflection attains a maximum value when the crack tip is at a distance of  $\approx d/4$  from the particle center. Interestingly, the crack deflection keeps increasing even after the crack tip grows past the particle centerline. Maximum crack deflection occurs when the crack travels across the inclusion and propagates  $d/2$  away from the inclusion center. With further crack propagation a slight reversal of angle of deflection can be seen and the crack travels towards the line-of-symmetry with a relatively small angle. Also it can be noticed that the presence of a larger inclusion is felt earlier by the crack tip. The amount of crack deflection increases with the increase in inclusion size. Figure 8(b) shows the variation of maximum deflection from the line-of-symmetry with inclusion diameter. For an eccentricity of  $d/2$ , plot suggests that the maximum deflection varies monotonically (with slight non-linearity) with inclusion size.

The inclusion size effect on ERR is shown in Fig. 8(c). Plots show the variation of  $G/G_0$  with  $a/W$  for various inclusion sizes. The size effect in terms of decreasing ERR is evident for all inclusion sizes. As one would expect, the effect can be noticed much earlier as the particle size increases. The largest among the chosen inclusions shows the lowest non-dimensional ERR, while in case of smallest inclusion the crack propagates with  $G/G_0 \approx 1$  until a length of  $a/W \approx 0.40$ . For all inclusion sizes  $G/G_0$  decreases when the crack propagates

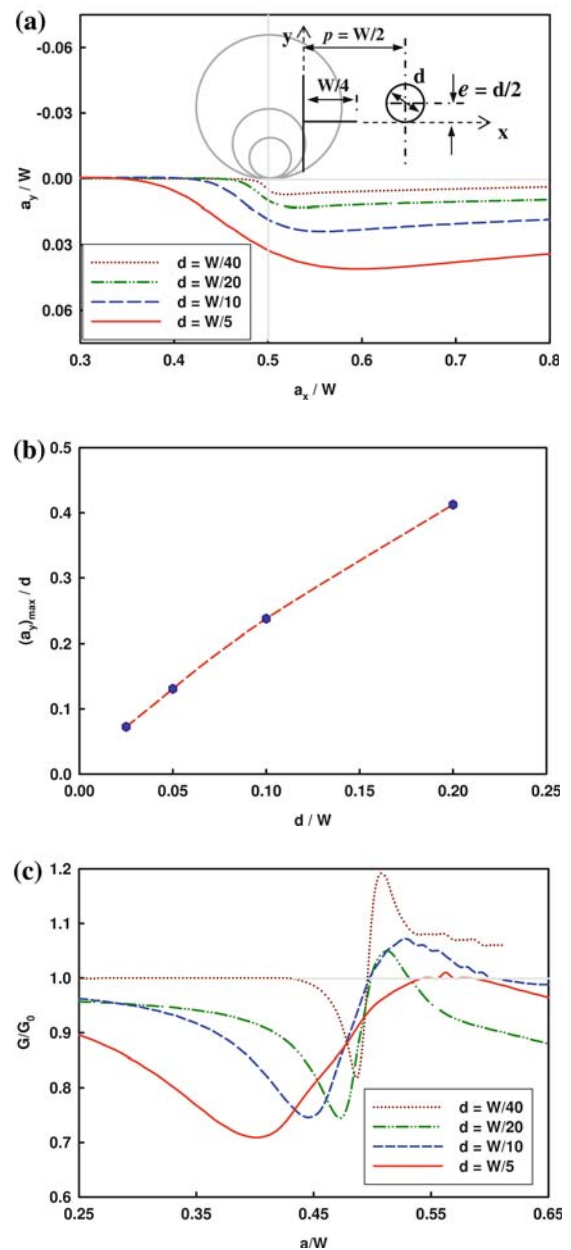


**Fig. 8** Role of particle size on crack deflection and ERR: (a) crack deflection in the presence of inclusions of various diameters for a fixed eccentricity  $e = d/2$ ; (b) variation of maximum crack deflection from the line-of-symmetry with inclusion diameter; (c) variation in non-dimensional ERR with  $a/W$

towards the inclusion, which attains a minimum when the crack tip is at a distance of  $d/2$  from the inclusion centerline. This is similar to the results obtained in case of crack-tip shielding and inclusion eccentricity effects. With further crack propagation  $G/G_0$  increases

and reaches a maximum just before it travels  $d/2$  across the center of the inclusion. This is followed by a monotonic but gradual decrease in  $G/G_0$ . Similar to the previous results, for all inclusion sizes greater shielding occurs while the crack is traveling towards the inclusion compared to the amplification effect while receding from the inclusion. Also from the plots it can be noticed that these effects increase with an increase in inclusion size.

### 3.5 Crack propagation through particle clusters

Next, simulations of crack growth through idealized clusters of particles in a brittle and compliant matrix is undertaken. In a typical particulate composite secondary phase is randomly distributed in a matrix at a known volume fraction. In the present work, this situation is approximated using a particle-cluster. Particle distribution, particle size, inter particle distance (cluster radius), and cluster orientation relative to the initial crack orientation, are some of the parameters which can be used to characterize a cluster. In this study, a six-particle-cluster (see Fig. 9(a)) with a centrally located particle surrounded by five others at the corners of a uniform pentagon is used. Unlike square, hexagonal or octagonal arrangements of particles, this pattern captures randomness of fillers in a matrix to a greater degree while being characterized by a few simple parameters. In the current study, a single cluster is positioned ahead of a crack tip in the loading geometry used earlier. The cluster geometry for a chosen particle diameter  $d$  is defined in terms of (i) distance between particles on the periphery and the center one (cluster radius  $R$ ) and (ii) the smallest angle ( $\theta$ ) of the surrounding particles from the line-of-symmetry, as shown in the figure. Clearly, the crack particle cluster interaction and its effects on crack path and ERR depend on the cluster orientation  $\theta$  and a measure of volume fraction, which are investigated next.

#### 3.5.1 Effect of cluster orientation

As the propagating crack negotiates various members of a particle-cluster, the crack path become tortuous causing greater energy dissipation and higher overall fracture toughness compared to a neat matrix. In this context, it is interesting to address the effect of parti-

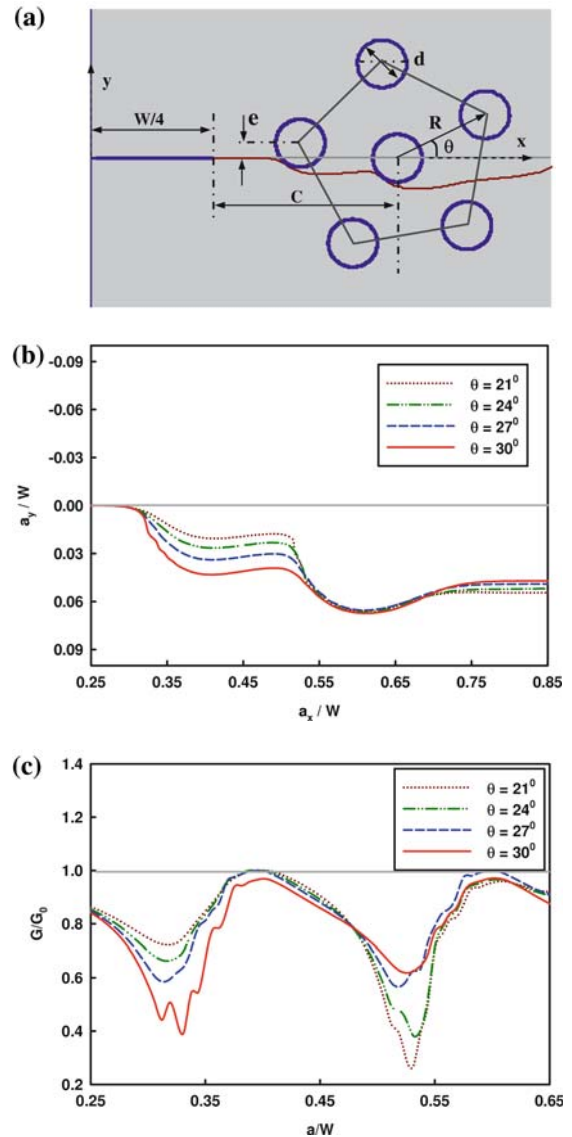


**Fig. 9** Interaction between a crack and a particle cluster with a pentagonal arrangement: (a) cluster orientation is defined in terms of  $\theta$ . Crack path in the presence of particle cluster is shown; (b) crack deflection in the presence of particle cluster of various orientations; (c) variation of ERR with  $a/W$  showing the effect of cluster orientation

cle arrangement such as cluster orientation relative to the initial crack impingement. Accordingly, the role of angular parameter  $\theta$  (see Fig. 9(a)) on crack growth behavior through a particle cluster is studied next. In these simulations, the center of the cluster is considered to be located at a distance of  $C/W \approx 0.4$  where  $C$  is the distance of the center of the inclusion from the

initial crack tip. The cluster radius is considered as  $2d$ ,  $d$  being the inclusion diameter. The angle  $\theta$  is varied from  $21^\circ$  to  $33^\circ$  for the pentagonal arrangement used here. Figure 9(b) shows the crack propagation for various cluster orientation angles. Evidently, significant crack path deflections within the cluster can be noticed from the figure. The crack deflection from the first particle influences the subsequent growth towards the second and so on. The crack, already deflected away from the line-of-symmetry of the cluster at the first interaction, undergoes further deflection due to the central particle of the cluster. As the crack propagates further and away from the central particle, the effect of next neighboring particles can be noticed. The differences in crack paths are greatest when the crack interacts with the first particle of the cluster. That is, crack deflection increases monotonically with increasing angular parameter  $\theta$ . The opposite trend is evident when the crack reaches the central particle—the crack deflection at the central particle of the cluster decreases with  $\theta$ . Once the crack recedes from the central particle, all crack paths essentially coincide as the crack leaves the cluster. These observations suggest that, the net effect of the angular parameter  $\theta$  on cumulative crack deflection is small even though crack paths within the cluster are significantly different.

The above observations can be further quantified in terms of ERR for each crack path corresponding to different values of  $\theta$ . The effect of the change in  $\theta$  on ERR is shown in Fig. 9(c). Nondimensional ERR is plotted against  $a/W$  for various cluster orientations. Plots show significant variation in  $G/G_0$  as the crack propagates and interacts with surrounding particles. Interestingly, ERR values for all cluster orientations are lower when compared to the case of unfilled (neat) matrix material. This suggests lowering of crack tip stress intensification as various elements of the cluster are encountered by the crack resulting in an overall increase in fracture toughness of the material. The cluster orientation affects crack propagation and hence  $G/G_0$  differently. As can be seen from the plots that for  $30^\circ$  orientation, the first particle interaction gives lowest  $G/G_0$ , while for the case of  $21^\circ$  orientation the center particle in the cluster affects  $G/G_0$  the most. For other orientations, the values of  $G/G_0$  are bounded by the values for these two cases. In order to estimate which cluster orientation dissipates the most energy, average value of nondimensional ERR ( $ERR_a$ ) for each case is determined. Here,  $ERR_a$  is defined as,

$$ERR_a = \frac{1}{(a/W)} \int \frac{G}{G_0} d \left( \frac{a}{W} \right). \quad (13)$$

The  $ERR_a$  for the crack propagation between  $a/W = 0.25$  and  $0.70$  has been evaluated. For the chosen cluster orientations  $21^\circ$ ,  $24^\circ$ ,  $27^\circ$  and  $30^\circ$ , the  $ERR_a$  values are 0.83, 0.83, 0.84 and 0.80, respectively. Thus, it can be again be concluded that the effect of cluster orientation has negligible effect on energy dissipation.

### 3.5.2 Effect of cluster volume fraction

The effect of particle volume fraction on crack growth is considered next. This can be done by changing either the cluster radius ( $R$ ) and keeping the particle size ( $d$ ) constant or by changing the particle size and keeping the cluster radius constant. To avoid particle size effects, an investigation is performed for various cluster radii with a fixed particle size.<sup>3</sup> It has already been shown in the previous section that cluster orientation has only a small effect on ERR. Therefore the cluster orientation is chosen such that the central particle of the cluster is located symmetrically at  $C/W \approx 0.4$  relative to the initial crack tip and the particle nearest to the initial crack tip has  $d/\beta$  eccentricity ( $e$ ) as shown in Fig. 9(a). Defining a control volume to find volume fraction is not straight forward for the chosen pentagonal cluster arrangement because it cannot be replicated symmetrically in all directions. Therefore instead of volume fraction, a parameter ‘area ratio’ is defined for quantification purpose. The area ratio, AR, is defined as the ratio of the total area occupied by the particles inside the pentagon to the total area of the pentagon itself.

Figure 10(a) shows crack deflections in the presence of particle cluster for 10% to 25% area ratios. Similar but distinct crack paths can be seen for various values of AR. As with the cluster orientation study, crack paths show dependency on the value of AR. Earlier crack deflection can be noticed for the case of 10% AR due the presence of a particle much closer to the initial crack tip when compared to other AR values. With an increase in AR, the crack deflections occur at different  $a/W$  values sequentially. The first interaction is the

<sup>3</sup>  $\frac{C}{W} = \frac{3}{40}$  in this case. A different particle diameter is chosen compared to the previous computations so that simulations can still be performed for lower volume fractions without the cluster geometry interfering with the initial crack tip.

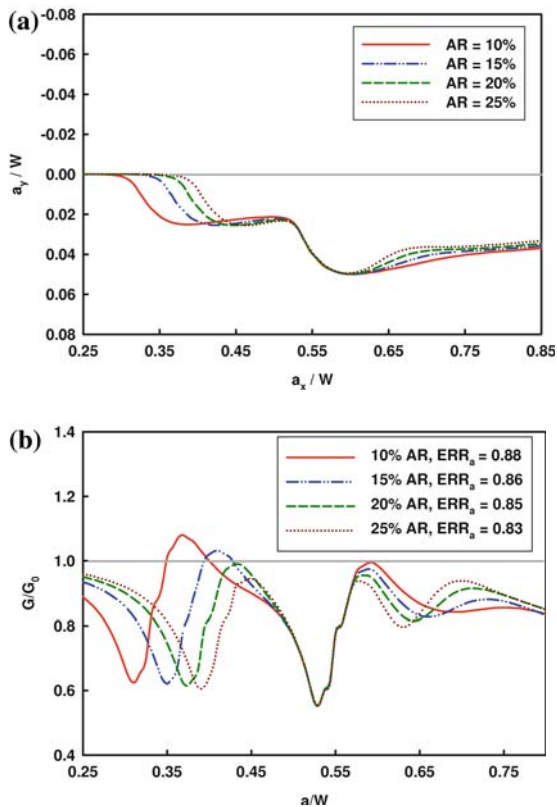


**Fig. 10** Interaction of a crack with a particle cluster to study the effect of volume fraction: (a) crack deflection for various volume ratios; volume ratio is changed by expanding the cluster radius  $R$  shown in Fig. 9(a); (b) variation of energy release rate with crack growth

only dominant distinguishing feature among the different crack paths. The paths tend to merge while propagating around the central inclusion. That is, the crack trajectory is essentially same between  $a/W \approx 0.54$  and  $0.60$  in the figure. With further crack propagation the paths show variation with AR. The distinct crack paths beyond  $a/W \approx 0.60$  are due to the difference in surrounding inclusion locations. Interestingly, when compared to the crack deflection in the presence of a single particle (Figs. 6(a), 8(a)), prominent and higher crack deflection can be noticed for the cluster for all values of AR.

Figure 10(b) shows the variation of nondimensional ERR with  $a/W$  for various area ratios. A combined effect of crack tip shielding and amplification, particle size effect and particle eccentricity with respect to propagating crack can be seen in terms of distinct  $G/G_0$  variation for different ARs. For lower AR values the

decrease in ERR can be noticed earlier due to the proximity of initial crack tip to the nearest particle. But this also gives rise to an early amplification as the crack propagates away from the particle. The amplification effect is more prominent for lower AR values due to its larger inter-particle separation distance. In case of higher ARs, however, the amplification effect is relatively suppressed due to the proximity of next neighboring particle. When a crack negotiates the first peripheral particle of the cluster, the lowest  $G/G_0$  occurs at different  $a/W$  values depending upon the particle location with respect to the initial crack tip. Even though the plots show distinct variations of  $G/G_0$  for various ARs when a crack propagates around its first encounter, they all tend to follow the same path as the central particle is approached. For all values of AR, nearly the same  $G/G_0$  variation between  $a/W = 0.5$  and  $0.58$  is evident. Further crack propagation shows the effect of next neighboring particle effect on  $G/G_0$ , where again lowest  $G/G_0$  occurs at different  $a/W$  depending upon the particle location. This is followed by some increase in  $G/G_0$  similar to the amplification effect, and then a monotonic but gradual decrease in  $G/G_0$ .

Here again the area ratio effect is quantified using average ERR,  $ERR_a$ , defined earlier in Eq. (13). A crack propagates different distances within the particle cluster due to different cluster radius for each AR. Hence, the same crack propagation length can not be used to evaluate  $ERR_a$ . Subsequently, a crack propagation length of  $2R$  within the particle cluster is considered for comparison. For 10%, 15%, 20% and 25% AR values, the  $ERR_a$  values have been calculated as 0.88, 0.86, 0.85 and 0.83 respectively. A monotonic decrease in  $ERR_a$  with increase in AR can be noticed. This in turn suggests that the material becomes relatively more resistant to crack propagation with increase in volume fraction of secondary phase rigid fillers.

#### 4 Concluding remarks

An SGBEM-based tool is developed to simulate crack growth in a heterogeneous brittle material system. Simulations are performed to study crack paths and to compute SIFs under plane stress conditions. The quasi-static crack-growth prediction tool is first bench marked and simulations are performed to examine the particle

size, eccentricity and the shielding effects on crack growth in the presence of isolated inclusions. In these simulations the secondary phases are assumed to be perfectly bonded to a brittle and relatively compliant matrix. Subsequently, crack growth through idealized particle clusters of uniform pentagonal arrangement are studied. The results are summarized as follows:

- A propagating crack is affected by a rigid inclusion in terms of energy release rate ahead of visible crack deflection. That is, ERR values are affected when the crack is a few inclusion diameters ( $d$ ) away from it. On the other hand crack deflection is noticeable only when the crack is  $\leq 3d/2$  from the center of the inclusion while approaching it. For both symmetric and eccentric inclusions (with respect to the initial crack orientation), the energy release rate is minimum when the crack tip is at a distance of  $\approx d/2$  from the center of the inclusion. As eccentricity increases, the crack deflection decreases while the energy release rate increases.
- Crack tip shielding and amplification increase with decrease in inter particle separation distance in a particle-pair arranged symmetrically relative to the crack. For an eccentrically arranged particle-pair, on the other hand, the crack tip shielding is greater when compared to the symmetric case. However, eccentricity has negligible effect on amplification. In general, shielding effects are greater than amplification effects when a crack propagates around a particle.
- Crack deflection increases and the energy release rate decreases with increase in particle size when the size of the reinforcement is in the range  $d/W = 2-20\%$ . A propagating crack is influenced by a larger particle in front much earlier than the smaller ones. Yet, the crack deflection is relatively unaffected by the inclusion when the tip is at a distance of  $\geq 3d/2$  from the center of the inclusion.
- A crack propagating through a particle cluster shows distinct crack trajectories for various cluster orientations. The cluster orientation, however, has negligible effect on overall energy dissipation.
- The crack path depends upon the cluster area ratio, AR. The total energy dissipation decreases with increase in cluster AR. This suggests that the material becomes more resistant to the crack propagation for higher area ratios.

**Acknowledgements** This research was supported in part by the U.S. Army Research Office Grant #W911 NF-04-1-0257 to HVT and A-VP, and by the Applied Mathematical Sciences Research Program of the Office of Mathematical, Information, and Computational Sciences, the U.S. Department of Energy under contract DE-AC05-00OR22725 with UT-Battelle, LLC., to TK. The authors would also like to thank Dr. Len Gray (ORNL) for his contribution to the SGBEM codes used in this work.

## References

- Anderson TL (1995) *Fracture Mechanics, Fundamentals and Applications*. CRC Press
- Atkinson C (1972) The interaction between a crack and an inclusion. *International Journal of Engineering Science* 10:127–136
- Barsoum RS (1976) On the use of isoparametric finite elements in linear fracture mechanics. *Int J Numer Meth Eng*, 10:25–37
- Bonnet M (1995) *Boundary Integral Equation Methods for Solids and Fluids*. John Wiley & Sons, England
- Bonnet M, Maier G, Polizzotto C (1998) Symmetric Galerkin boundary element method. *ASME Appl Mech Rev* 51: 669–704
- Bush MB (1997) The interaction between a crack and a particle cluster. *Int J Fract* 88:215–232
- Erdogan C, Gupta GD, Ratwani M (1974) Interaction between a circular inclusion and an arbitrary oriented crack. *J Appl Mech (Trans ASME)* Dec:1007–1013
- Erdogan F, Sih GC (1963) On the crack extension in plates under plane loading and transverse shear. *J Basic Eng* 86:519–527
- Faber KT, Evans AG (1983) Crack deflection process - I. Theory. *Acta Mater* 31:565–576
- Ferber F, Hinz O, Herrmann K. (1993) Numerical and experimental modelling of crack systems in homogeneous and nonhomogeneous solids. In: C.A. Brebbia and G.M. Carlomagno (eds) *Computational Methods and Experimental Measurements VI, Vol. 2: Stress Analysis*. CMP, Southampton Boston/Elsevier, pp 259–276
- Gray LJ (1991) Evaluation of hypersingular integrals in the boundary element method. *Math Computer Model* 15: 165–174
- Gray LJ, Paulino GH (1998) Crack tip interpolation, revisited. *SIAM J Appl Math* 58:428–455
- Gray LJ, Phan A-V, Paulino GH, Kaplan T (2003) Improved quarter-point crack tip element. *Eng Fract Mech* 70: 269–283
- Haddi A, Weichert D (1998) Three-dimensional interaction between a crack front and particles. *Int J Numer Meth Eng* 42:1463–1476
- He MY, Hutchinson JW (1989) Crack deflection at an interface between dissimilar elastic material. *Int J Solids Struct* 25(9):1053–1067
- Henshell RD, Shaw KG (1975) Crack tip finite elements are unnecessary. *Int J Numer Meth Eng* 9:495–507
- Hwu C, Liang YK, Yen WJ (1995) Interactions between inclusions and various types of cracks. *Int J Fract* 73:301–323
- Kitey R, Tippur HV (2005a) Role of particle size and filler-matrix adhesion on dynamic fracture of glass-filled epoxy. I. Macro-mechanisms. *Acta Mater* 53:1153–1165

- Kitey R, Tippur HV (2005b) Role of particle size and filler-matrix adhesion on dynamic fracture of glass-filled epoxy. II. Linkage between macro- and micro-measurements. *Acta Materialia* 53:1167–1178
- Knight MG, Wrobel LC, Henshall JL, De Lacerda LA (2002) A study of the interaction between a propagating crack and an uncoated/coated elastic inclusion using the BE technique. *Int J Fract* 114:47–61
- Lei J, Wang Y-S, Gross D (2005) Analysis of dynamic interaction between an inclusion and a nearby moving crack by BEM. *Engineering Analysis with Boundary Elements*, 29:802–813
- Li R, Chudnovsky A (1993) Variation of the energy release rate as a crack approaches and passes through an elastic inclusion. *Int. J. of Frac.* 59: R69–R74
- Li R, Chudnovsky A (1993) Energy analysis of crack interaction with an elastic inclusion. *Int J Fract* 63: 247–261
- Lipetzky P, Knesl Z (1995) Crack-particle interaction in two-phase composites part II: crack deflection. *Int J Fract* 73: 81–92
- Lipetzky P, Schmauder S (1994) Crack-particle interaction in two-phase composites part I: Particle shape effects. *Inter. J. of Frac.* 65:345–358
- Martin PA, Rizzo FJ (1996) Hypersingular integrals: how smooth must the density be? *Int J Numer Meth Eng*, 39:687–704
- Moloney AC, Kausch HH, Kaiser, T, Beer HR (1987) Review — parameters determining the strength and toughness of particulate filled epoxide resins. *J. Mater. Sci.* 22: 381–393
- Nakamura Y, and Yamaguchi M (1992) Effects of particle size on the fracture toughness of epoxy resin filled with spherical silica. *Polymer* 33(16): 3415–3426
- Nakamura Y, Okabe S, Iida T (1999) Effects of particle shape, size and interfacial adhesion on the fracture strength of silica-filled epoxy resin. *Polymers Polymer Composites* 7(3):177–186
- Rizzo FJ (1967) An integral equation approach to boundary value problems of classical elastostatics. *Quart Appl Math* 25: 83–95
- Sendeckyj GP (1974) Interaction of cracks with rigid inclusions in longitudinal shear deformation. *Int J Fract* 10: 45–52
- Sih GC (1974) Strain energy density factor applied to mixed mode crack problems. *Int J Fract* 10:305–321
- Spanoudakis J, Young RJ (1984a) Crack propagation in a glass particle-filled epoxy resin, Part 2 Effect of particle-matrix adhesion. *J. Mater. Sci.* 19: 487–496
- Spanoudakis J, Young RJ (1984b) Crack propagation in a glass particle-filled epoxy resin, Part 1 Effect of particle volume fraction and size. *J Mater Sci* 19:pp. 473–486
- Tamate O (1968) The effect of a circular inclusion on the stresses around a line crack in a sheet under tension. *Int J Fract* 4:257–265
- Wang C, Libardi W, Baldo JB (1998) Analysis of crack extension paths and toughening in a two phase brittle particulate composite by the boundary element method: *Int J Fract* 94:177–188